

Probing the Unique Role of Gallium in Amorphous Oxide Semiconductors through Structure–Property Relationships

Stephanie L. Moffitt, Qimin Zhu, Qing Ma, Allison F. Falduto, D. Bruce Buchholz, Robert P. H. Chang, Thomas O. Mason, Julia E. Medvedeva,* Tobin J. Marks,* and Michael J. Bedzyk*

This study explores the unique role of Ga in amorphous (a-) In–Ga–O oxide semiconductors through combined theory and experiment. It reveals substitutional effects that have not previously been attributed to Ga, and that are investigated by examining how Ga influences structure–property relationships in a series of pulsed laser deposited a-In–Ga–O thin films. Element-specific structural studies (X-ray absorption and anomalous scattering) show good agreement with the results of ab initio molecular dynamics simulations. This structural knowledge is used to understand the results of air-annealing and Hall effect electrical measurements. The crystallization temperature of a-IO is shown to increase by as much as 325 °C on substituting Ga for In. This increased thermal stability is understood on the basis of the large changes in local structure that Ga undergoes, as compared to In, during crystallization. Hall measurements reveal an initial sharp drop in both carrier concentration and mobility with increasing Ga incorporation, which moderates at >20 at% Ga content. This decline in both the carrier concentration and mobility with increasing Ga is attributed to dilution of the charge-carrying In–O matrix and to increased structural disorder. The latter effect saturates at high at% Ga.

1. Introduction

The discovery of high carrier mobility in oxide films deposited at room temperature, ZnO^[1] and amorphous In–Ga–Zn–O (a-IGZO),^[2] stimulated intense academic and industrial research efforts aimed at exploring a-IGZO as a channel layer material for thin film transistors (TFTs).^[3] The wide band gap and ionic bonding of amorphous transparent conducting oxides (a-TCOs) sets this class of materials apart from other amorphous materials.^[4] The isotropic conduction orbitals of a-IGZO provide a marked charge transport advantage over the heretofore most common low-temperature semiconductor, amorphous (a-)Si. This advantage is rooted in the resilient s-state conduction manifold of a-IGZO; mobility is only minimally degraded by the bond disorder of the amorphous state. By contrast, a two to

three order-of-magnitude decline in mobility occurs upon the transition from crystalline Si to a-Si.^[3c,5] Note that amorphous indium oxide (a-IO) often serves as the matrix material for oxide semiconductors, but is not a viable TFT device material on its own. a-IO has low thermal stability and high carrier concentrations, which lead to unacceptably high off-state currents for TFT channel layer applications.^[6] To optimize the properties of a-IO the common practice, originating empirically, has been to add both Ga and Zn.^[4b,7] Although these modifying cations improve the TFT performance of a-IO, a fundamental mechanistic understanding of how these cation modifiers influence amorphous oxide properties is currently unresolved.

This study focuses on isolating the influence of Ga, which is rarely studied in the absence of Zn. The simpler two-cation system a-In–Ga–O (a-IGO) is employed here to elucidate the role of Ga in the thermal stability, carrier formation, and carrier mobility of a-IGO. Each property is explored across a range of a-IGO compositions to illuminate composition-property trends. These property trends are then understood in the context of an in-depth structural study. Although amorphous oxides lack long-range order, previous studies have established the persistence of local-scale order,^[8] and the use of element-specific local structure techniques, specifically X-ray absorption spectroscopy and X-ray scattering, has proven to be an incisive tool for understanding the structures of amorphous materials.^[9] The present investigation successfully couples these


Dr. S. L. Moffitt, Dr. Q. Zhu, A. F. Falduto, Dr. D. B. Buchholz, Prof. R. P. H. Chang, Prof. T. O. Mason, Prof. T. J. Marks, Prof. M. J. Bedzyk
Department of Materials Science and Engineering
and the Materials Research Center
Northwestern University
Evanston, IL 60208, USA
E-mail: t-marks@northwestern.edu; bedzyk@northwestern.edu

Dr. Q. Ma
DND-CAT
Northwestern Synchrotron Research Center
at the Advanced Photon Source
Argonne, IL 60439, USA

Prof. J. E. Medvedeva
Physics Department
Missouri University of Science & Technology
Rolla, MO 65409, USA
E-mail: juliaem@mst.edu

Prof. T. J. Marks
Department of Chemistry
Northwestern University
Evanston, IL 60208, USA

Prof. M. J. Bedzyk
Department of Physics and Astronomy
Northwestern University
Evanston, IL 60208, USA

 The ORCID identification number(s) for the author(s) of this article can be found under <https://doi.org/10.1002/aelm.201700189>.

DOI: 10.1002/aelm.201700189

X-ray techniques with *ab initio* molecular dynamics (MD) simulations. The close agreement achieved between theory and experiment surpasses previous reports^[10] and provides a comprehensive understanding of the a-IGO structure, which in turn provides an unprecedented description of how Ga influences the structure–property relationships at play in a-IGO.

Thermal stability in amorphous oxides refers to the tendency of these materials to resist the onset of crystallization. To maintain competitive TFT mobility, amorphous oxide semiconductors (AOSs) must avoid nano- or microinclusions of crystallites that act as scattering centers.^[8a,c] Small inclusions of crystalline phase always occur at the onset of crystallization. Thus, a sufficiently high crystallization temperature (T_{cryst}) is important to provide a thermal window for postdeposition processing without initiating crystallization. Substitutional cations have been shown to inhibit crystallization during postdeposition annealing as well as crystalline-phase growth from vapor or solution phases.^[8d,11] However, an understanding of which cations inhibit crystallization and why, is lacking. The results of the present study show that Ga substitution alone is capable of significantly increasing the T_{cryst} of a-IO. The present structural studies clearly reveal that substitutional Ga cations displace the amorphous structure farther away from thermodynamic equilibrium, and that to undergo crystallization, large changes must occur in the oxygen coordination and bonding around the Ga cations.

The channel layer of a TFT requires a semiconductor with low carrier density, so that control of carrier concentration is imperative. There is a growing consensus that the predominant point defect species responsible for carrier generation in a-TCOs are doubly charged oxygen vacancies.^[9,22–25] Experimental studies of a-IZO^[22,23] and a-IGZO^[25] have shown that in both cases the $d(\log \text{conductivity})/d(\log p\text{O}_2)$ slope is observed to be $-1/6$, which is consistent with doubly charged oxygen vacancies as the carrier generating species. The modifying role of Ga is typically defined in reference to the reduction of free carriers due to its high ionic potential and strong oxygen binding affinity.^[4b,12] Here, using theoretical modeling, we probe deeper to show that the true role of Ga in carrier production is twofold: (1) Ga decreases carrier density because

the Ga–O polyhedra do not contribute to carrier generation, and (2) Ga cations impede the clustering of undercoordinated In–O polyhedra, the source of free carriers. In addition, Ga_2O_3 has a larger optical band gap (4.8 eV) as compared to that in In_2O_3 (3.6 eV), hence, the band gap, as well as the location of the band edge, are tunable in IGO.^[13]

Several different models have been proposed to simulate the nature of carrier mobility in amorphous oxide films.^[12e,14] The challenge is that those factors which limit mobility can vary with growth conditions, such as temperature,^[8d] and affect film quality.^[2,14d,15] As this work emphasizes, film quality and TFT performance are tied to the structure of the film. Here we use the well-developed experimental and theoretical understanding of structure to discuss the nature of conduction and the role of Ga in the mobility of a-IGO. The agreement between experimental results and our model structure provides confidence in the electronic calculations. We show that Ga increases percolation barriers and trap states, as well as increases the range of hopping centers, which negatively affect both band conduction and variable range carrier hopping in the system. By focusing on the relationship between structure and transport barriers, we provide insight into the role of Ga in the mobility of not only the films in this work, but also the trends seen a-IGO TFT device performance.^[11b,16]

2. Results and Discussion

2.1. Thermal and Structural Properties

In the present study, measurements of T_{cryst} were performed for a series of a-IGO films with varying levels of Ga substitution. The T_{cryst} of a-IO is found to be 125 °C (Figure 1A), which agrees well with previously published results.^[6] With 8 at% Ga substitution (IGO8), the T_{cryst} rises to 250 °C. The maximum measured T_{cryst} is 425 °C for 51 at% Ga (IGO51), with the trend of increasing T_{cryst} with increasing Ga substitution clearly established. All films crystallize in the cubic- $\text{Ia}\bar{3}$ bixbyite phase, labeled $c\text{-In}_2\text{O}_3$ (Figure S1, Supporting Information). No secondary phases, such as $\beta\text{-Ga}_2\text{O}_3$, are evidenced in the final

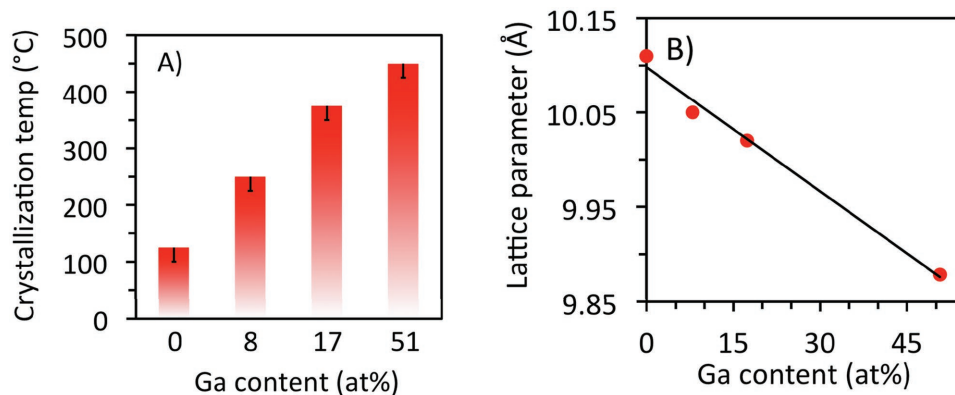


Figure 1. A) Crystallization temperature as a function of at% Ga substitution determined through 1 h anneal/quench/GIXRD cycles spaced 25 °C apart. Error bars represent the 25 °C window of uncertainty between pre- and postcrystallization runs. B) GIXRD determined lattice constant of the bixbyite unit cell for fully crystallized IGO samples as a function of Ga substitution. The solid line is a linear least-squares fit to the four data points. Error bars are smaller than the data points.

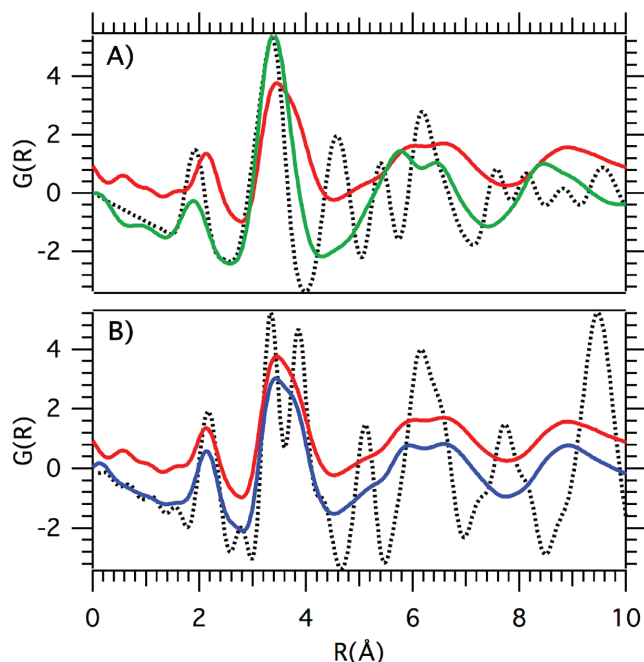


Figure 2. A) Pair distribution function (PDF) data for a-IGO with 17 at% Ga (red). Difference PDF of the structure around Ga in a-IGO17 (green). Calculated PDF for β -Ga₂O₃ is shown for reference (black dotted line). B) Measured PDF for a-IGO with 8 at% Ga (blue) and 17 at% Ga (red). Calculated PDF for bixbyite In₂O₃ is shown for reference (black dotted). The first and second peaks are produced by M–O and M···M distances, respectively. The first peak is weaker because O is a weak scatterer.

diffraction patterns. The lattice constants (Figure 1B) of the crystalline phases decrease linearly, in accord with Vegard's law, further suggesting that Ga is fully incorporated in the In–O matrix and does not phase-separate. The present lattice contraction, observed experimentally in this work, is in a good agreement with previous single-phase simulations of crystalline (c-) IGO films.^[17]

The lack of secondary phases in the present crystalline IGO films is surprising from a thermodynamics perspective. In the In₂O₃–Ga₂O₃ phase diagram^[24] the solubility of Ga in the bixbyite phase is only 5 at% at 1000 °C. This bulk phase

diagram suggests that given enough heat and time, the present films would devolve into two-phase structures. The absence of β -Ga₂O₃ in our high Ga-content (>5 at%) films highlights the difference between amorphous oxide thin films and bulk oxides. Clearly the amorphous films are only kinetically stable, not thermodynamically stable.

2.1.1. Experimental Structure

Anomalous-grazing-incidence wide angle X-ray scattering measurements (A-GIWAXS) also reveal the absence of phase separation in the IGO amorphous state (Figure 2A, green). From the difference pair distribution function (d-PDF)^[18] we see the structure around Ga does not correspond to that of β -Ga₂O₃ (Figure 2A, black). The position of the second shell peak is considerably larger than the Ga···Ga distance found in β -Ga₂O₃ (Figure 2A, black). In addition, the number and shape of the density fluctuations around Ga bear great similarity to those of the X-ray scattering derived PDF for the averaged structure (Figure 2A, red). These consistencies between the PDF and d-PDF results argue that a homogeneous distribution of Ga ions is achieved by the pulsed laser deposition (PLD) growth technique. These distributed Ga ions increase the overall structural disorder of the system. A comparison of the PDF of IGO8 (blue) and IGO17 (red) (Figure 2B) shows that as the Ga content increases from 8 to 17 at% there is a broadening of the PDF features, indicative of increased disorder. This disorder affects M···M distances and beyond.

Extended X-ray absorption fine structure (EXAFS) analyses of the present a-IGO samples were performed at both the Ga and In K-edges (Table 1). The fits reveal average coordination numbers (*N*) and bond distances (*R*). The local first shell structure of bixbyite (In₂O₃)^[19] and β -gallia (Ga₂O₃)^[20] derived from X-ray diffraction are presented as references. Crystalline In₂O₃ has a first shell (metal–oxygen, M–O) coordination number of 6. Crystalline β -gallia has two Ga–O coordination sites, half are *N* = 4 tetrahedral sites and the other half are *N* = 6 octahedral sites (Figure S3, Supporting Information). In a perfect crystal of β -gallia, this results in an average *N* of 5.

In the present study, all a-IGO samples show significant undercoordination of both In and Ga, compared to their

Table 1. First shell (metal–oxygen) EXAFS fitting results of experimental samples compared with room temperature MD simulations. *N* = Coordination number, *R* = bond distance, ECN = effective coordination number.

	Samples	<i>N</i>	<i>R</i> [Å]	Simulations	ECN	<i>R</i> [Å]
Ga local structure	c-Ga ₂ O ₃ (from XRD)	$5 = \frac{1}{2} \cdot 4 + \frac{1}{2} \cdot 6$	$1.93 = \frac{1}{2} \cdot 1.85 + \frac{1}{2} \cdot 2.01$			
	a-IGO8	4.25 ± 0.29	1.88 ± 0.014	a-IGO11	4.28	1.92
	a-IGO17	3.69 ± 0.28	1.90 ± 0.015	a-IGO19	4.38	1.93
	a-IGO51	4.14 ± 0.22	1.88 ± 0.011	a-IGO41	4.66	1.95
In local structure	c-In ₂ O ₃ (from XRD)	6	2.17			
	a-IO	5.11 ± 0.53	2.16 ± 0.018	a-IO	5.30	2.17
	a-IGO8	5.26 ± 0.56	2.16 ± 0.023	a-IGO11	5.20	2.17
	a-IGO17	5.11 ± 0.53	2.16 ± 0.026	a-IGO19	5.13	2.17
	a-IGO51	4.76 ± 0.53	2.17 ± 0.026	a-IGO41	5.13	2.17

respective pure crystalline references (Table 1). In addition, despite Ga being well dispersed in the In–O matrix, there is dissimilarity in the oxygen coordination around Ga versus In. In the amorphous films, the oxygen coordination number around In is ≈ 5 but around Ga it is much closer to 4. This trend is echoed in the fitting results of M–O bond distance. The average length of the Ga–O bond, 1.88 Å, is far shorter than the average In–O bond length, 2.16 Å. Note that the present EXAFS-derived 1.88 Å Ga–O bond length lies much closer to that for tetrahedral Ga (1.85 Å) than to that for octahedral Ga (2.01 Å). Assuming bond distance increases as average coordination number increases,^[21] a 1.88 Å Ga–O bond distance suggests <20% of the Ga sites are sixfold coordinate. All of the a-IGO films studied here show a minority of sixfold Ga sites. Note that Ga prefers the local coordination of its native oxide, β -Ga₂O₃ (a mixture of fourfold and sixfold coordination), over that of the amorphous indium oxide matrix, which clearly has a bixbyite-like structure at local- (Table 1; Figure S2A, Supporting Information) and medium-range distances (Figure 2).

The X-ray scattering measurements in this study provide independent experimental confirmation of the EXAFS results in Table 1. Figure 2B shows the PDFs obtained for two of the amorphous films, which are compared with the PDF calculated for the c-In₂O₃ reference. The first peak positions of the PDFs (Figure 2B) are composed of the weighted sum of the Ga–O and the In–O bond distances. The downward shift of the first peak from 2.14 Å for IGO8 to 2.12 Å for IGO17 is consistent with the increasing quantity of short Ga–O bonds as the Ga content increases. Figure 2A compares the PDF of IGO17, the d-PDF of IGO17 (the structure surrounding Ga), and the reference PDF of c-Ga₂O₃. The comparison highlights the departure of the Ga first-shell structure from the first-shell structure of the surrounding In–O matrix. The A-GIWAXS d-PDF (Figure 2A, green) demonstrates an average Ga–O bond length is 1.88 Å, in agreement with Table 1. Thus, both the EXAFS and A-GIWAXS/GIWAXS results find a departure of the Ga first-shell structure from the first-shell structure of the In–O matrix: both support the presence of low Ga–O coordination.

The tendency to maintain lower coordination within a higher coordinated matrix may contribute to the increased thermal stability of a-IGO over that of a-IO. Increased thermal stability has been reported in systems with Zn substituting for In, such as in a-IZO or a-ZITO (amorphous zinc indium tin oxide),^[11d,22] and systems with Zn substituting for Sn, a-ZTO (amorphous zinc tin oxide).^[23] The capacity of both Ga and Zn to raise the T_{cryst} of amorphous oxides suggests that the presence of distinctly low-coordinated sites suppresses long-range order. Additionally, as a-IGO films crystallize, Ga transitions to a significantly higher average coordination number and the Ga–O distance increase (Table 2). This observation strongly suggests that fourfold and fivefold coordinated sites must transition to sixfold coordinated sites for crystallization to occur. This transition is supported by the crystal structure of the crystalline films, bixbyite, which consists entirely of sixfold coordinated metal sites (Figure 1B). This increase in coordination number (ΔN), and the resultant increase in bond distance (ΔR), is far larger for Ga than for In. The increase in Ga coordination number upon crystallization is almost twice that of In. Additionally, the ΔR for the In–O bond distance is negligible, especially in comparison to the ΔR

Table 2. Comparison of first-shell (metal–oxygen) EXAFS fitting results of as-deposited (amorphous) versus annealed (crystallized) films, showing changes in coordination numbers and bond lengths. N = metal–oxygen coordination number. R = bond distance. ΔN and ΔR = the difference in coordination and bond distance between as-deposited and air-annealed samples.

	Samples	N	R [Å]	ΔN	ΔR [Å]
Ga K-edge	As-dep IGO8	4.25 ± 0.29	1.88 ± 0.014	1.39	0.15
	Anneal IGO8	5.64 ± 0.48	2.03 ± 0.021		
	As-dep IGO51	4.14 ± 0.22	1.88 ± 0.011	1.16	0.13
	Anneal IGO51	5.30 ± 0.63	2.01 ± 0.028		
In K-edge	As-dep IGO8	5.26 ± 0.41	2.16 ± 0.023	0.53	0.01
	Anneal IGO8	5.79 ± 0.53	2.17 ± 0.020		
	As-dep IGO51	4.76 ± 0.56	2.17 ± 0.026	0.82	0.01
	Anneal IGO51	5.58 ± 0.53	2.18 ± 0.021		

of the Ga–O bond. Thus, because of the capacity to maintain a unique local structure within a more highly coordinated matrix, Ga substitution creates a barrier to crystallization.

2.1.2. MD-Simulated Structure

The results of ab initio MD simulations support our experimental observations and provide further insight into the effect of Ga substitution on the structural properties of amorphous IGO. Specifically, in excellent agreement with our EXAFS results, Table 1, an analysis of the calculated first-shell structural characteristics shows, (i) the average In–O distance remains the same in all three a-IGO structures, 2.17 Å; and (ii) the average In–O coordination decreases slightly with increasing Ga content: 5.30, 5.20, 5.13, and 5.13 for amorphous In₂O_{2.96} (IO), In_{1.78}Ga_{0.22}O_{2.96} (IGO11), In_{1.63}Ga_{0.37}O_{2.96} (IGO19), and In_{1.19}Ga_{0.81}O_{2.96} (IGO41), respectively. The calculated distribution of In–O coordination numbers (Figure 3A) reveals that the presence of Ga suppresses the population of In atoms coordinated by 6 oxygen, i.e., those with the effective coordination number (ECN) = 5.7–6.0; whereas the number of undercoordinated In atoms (ECN = 4.0–5.0) increases with the Ga content. In agreement with the Ga K-edge EXAFS measurements, the Ga atoms in amorphous IGO are primarily fourfold-coordinated: the calculated average Ga–O coordination is 4.28, 4.38, and 4.66 for Ga substitutions of 11, 19, and 41 at%, respectively. The calculated distributions of Ga–O coordination (Figure 3B) suggest that with increasing Ga fraction, Ga atoms coordinated to 5 oxygen atoms (ECN = 4.5–5.0) begin to prevail, while Ga atoms coordinated with 6 oxygen atoms remain negligible. Accordingly, the Ga–O distances increase slightly, from 1.92 to 1.93 Å and to 1.95 Å for 11, 19, and 41 at% of Ga, respectively. These values are in agreement with the average Ga–O distance in β -gallia, 1.93 Å (Table 1), again showing that, in the amorphous phase, Ga prefers the local oxygen environment of pure Ga₂O₃ to that of the In–O matrix. Note that the effect of Ga on the local structure opposes the formation of nanocrystallites, composed of all M–O octahedra, observed at the onset of crystallization; the Ga–O octahedral population remains negligible while the In–O octahedral decrease in response to the Ga substitution.^[8a,c]

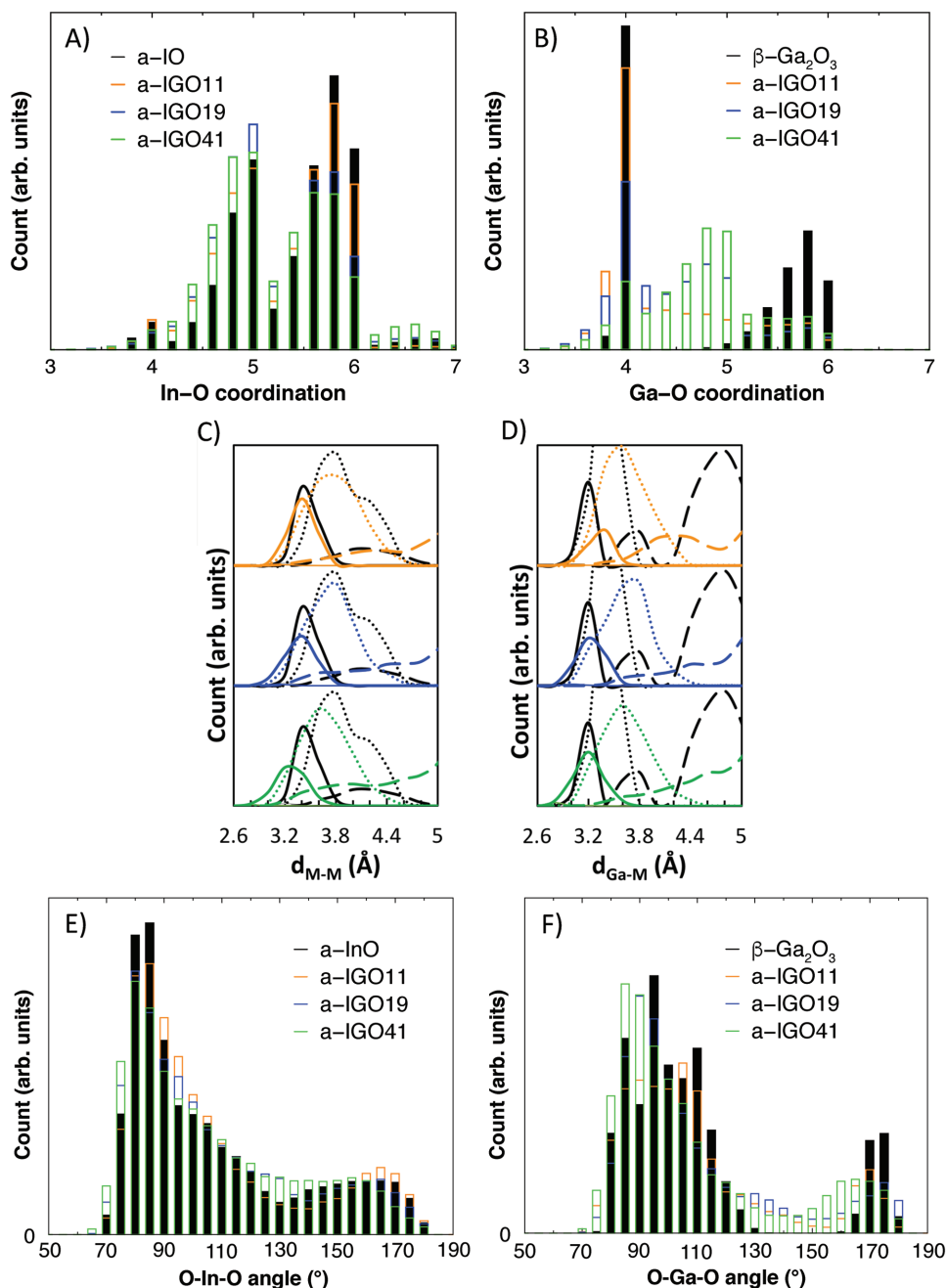


Figure 3. Distribution of calculated ECN values in a-IO and three a-IGO compositions as obtained from room temperature MD simulations for A) In–O and B) Ga–O. Spread of polyhedra edge-shared (solid line), corner-shared (dotted line), and lack of sharing (dashed line). C) M...M distances and D) Ga...M distances shown for a-IGO11 (orange), a-IGO19 (blue), and a-IGO41 (green). Black lines show the sharing distributions for a-IO in (C) and for β -Ga₂O₃ in (D). Distribution of calculated bond angle distributions for E) O–In–O and for F) O–Ga–O.

Evolution to 6-coordinate Ga may in principal impede crystallization for thermodynamic and/or kinetic reasons. A thermodynamic argument can be made using the In₂O₃-Ga₂O₃ phase diagram^[24] in which bulk In_{2-x}Ga_xO₃ has very limited solubility at the bixbyite/In₂O₃ side of the phase diagram,^[24] with only 5 at% Ga known to incorporate into bixbyite In₂O₃ before reaching the phase boundary, i.e., the solubility limit. Thus, having a large fraction of the Ga sites in a-IGO sixfold coordinated is thermodynamically unfavorable. A kinetic argument can also be

made by suggesting that there may be an activation barrier to the transition of Ga–O tetrahedra to octahedra. For this transition, from tetrahedral coordination to octahedral coordination, the film can either undergo a rearrangement of polyhedral connectivity or uptake oxygen (see the Supporting Information for elaboration). Previous work has shown that both oxygen uptake^[25] and structural rearrangement^[8c] are possible in In-based amorphous oxide films. Additionally, the multicoordinate nature of Ga cations renders the Ga–O coordination geometry

more sensitive to the O stoichiometry than does In–O coordination. From additional MD simulations of the amorphous oxide with lower O stoichiometry, $\text{In}_{1.19}\text{Ga}_{0.81}\text{O}_{2.92}$ (see the Supporting Information), it is found that the Ga–O coordination is reduced to 4.45, whereas the In–O coordination decreases only slightly to 5.09—as compared to ECN (Ga–O) = 4.66 and ECN (In–O) = 5.13 in $\text{In}_{1.19}\text{Ga}_{0.81}\text{O}_{2.96}$. These results are in accord with the observed higher sensitivity of the Ga–O coordination to annealing (Table 2)—the additional energy from heating the samples may promote O diffusion and enable long-range structural reconstruction; both factors facilitate the higher coordination of Ga. Clearly, additional energy is required for IGO versus IO crystallization because the system must dramatically increase M–O coordination to form the bixbyite phase.

Moreover, in accord with the observed trend in IGO crystallization temperature (Figure 1), the calculated distortions in the In–O polyhedra become more pronounced with increasing Ga fraction: the average variance of the first-shell In–O distances is $8.42 \times 10^{-3} \text{ \AA}^2$, $9.55 \times 10^{-3} \text{ \AA}^2$, $10.74 \times 10^{-3} \text{ \AA}^2$, and $11.64 \times 10^{-3} \text{ \AA}^2$ for amorphous IO, IGO11, IGO19, and IGO41, respectively. The Ga–O polyhedra are also strongly distorted with the average variance for the Ga–O distances of $1.40 \times 10^{-2} \text{ \AA}^2$, $1.89 \times 10^{-2} \text{ \AA}^2$, and $1.66 \times 10^{-2} \text{ \AA}^2$ for IGO11, IGO19, and IGO41, respectively, being larger than those for the corresponding In–O distances reported above. The O–In–O and O–Ga–O angle distributions given in Figure 3E,F also illustrate the strong polyhedral distortions. This result may at first appear counterintuitive given the fact that the Ga–O bonding is stronger than the In–O bonding. However, we believe that the strong local distortions in Ga–O polyhedra stem from their intrinsic multicoordinate nature (4- and 6-coordinate in monoclinic $\beta\text{-Ga}_2\text{O}_3$); in addition, the weaker metal–O bonding of the host In atoms facilitates the coordinative transformations for Ga. Thus, the presence of Ga increases disorder in the M–O bonding and moves the system farther away from an ordered crystalline lattice.

Medium-range structural characteristics, i.e., how the M–O polyhedra combine to form a network, plays a crucial role in amorphization.^[8c] Connectivity or O sharing between the M–O polyhedra having different coordination patterns and degrees of distortion determines their spatial distribution and, hence, governs the structural reorganization, crystallization, and phase formation phenomena. In bixbyite In_2O_3 , the second and third shells of In are associated with 6 In neighbors at 3.3 Å that share two O atoms with the central In atom (i.e., the corresponding polyhedra are edge-shared) and 6 In neighbors at 3.8 Å that share one oxygen atom (corner-shared polyhedra). In the amorphous phase, a significant amount of edge-shared connections become corner-shared, Figure 3C: out of the total number of all In–In pairs that share 1, 2, or 3 O atoms, as many as 80% share only a single O atom.^[8c,26] As a result, the distance distribution for the corner-sharing connections in undoped a-IO is nearly twice as wide as that in crystalline In_2O_3 , overlapping significantly with the distance distribution for the edge-shared In···In pairs (Figure 3C). In a-IGO, both the edge- and corner-shared distributions shift toward shorter metal–metal (M···M) distances in agreement with the small ionic size of Ga. Significantly, addition of Ga broadens the edge-sharing distribution so

that it overlaps completely with the corner-sharing distribution for the Ga fraction of 19% and above (Figure 3D). Experimentally, the second and third shells cannot be distinguished in this case but, the comparatively shorter Ga···M distances, as compared to M···M distances, can be seen in the comparison of the PDF and d-PDF (Figure 2A). Thus, the stronger local distortions caused by the capacity of Ga cations to assume different O environments than the surrounding In–O matrix and the higher medium-range disorder in a-IGOs with increased Ga content contribute to the observed increase in the crystallization temperature in these oxides.

2.2. a-IGO Electrical Properties

To investigate the influence of Ga substitution on the electrical properties of the present PLD-deposited a-IGO films, a systematic Hall effect study as a function of Ga content was carried out at room temperature, and the results are shown in Figure 4A. Note that the growth conditions of all films represented in Figure 4 were identical. The $\approx 75\%$ fall electrical conductivity is consistent with the relatively modest decline in carrier content ($\approx 25\%$) and the drop in carrier mobility of $\approx 50\%$. All three properties approach constancy beyond a Ga content of 18 at%.

2.2.1. Carrier Generation: Experimental

The change in the n-type carrier content upon Ga substitution is less than one order of magnitude, indicating that Ga is not a major source of carriers. At 10 at% doping and beyond, the Ga concentration is $\approx 10^{22} \text{ cm}^{-3}$, two orders of magnitude greater than the measured carrier density. The lack of carrier response is in contrast to crystalline systems, such as Zn–Ga–O where Ga is an effective dopant.^[4a,27] Additionally, In and Ga K-edge XANES (X-ray absorption near-edge) data (Figure S2, Supporting Information) comparing a-IGO films with reference oxides shows that both Ga and In maintain the same formal valence (3^+). Thus, Ga is isovalent with In and produces neutral “defects” that do not affect the electroneutrality condition. Next, a 51 at% Ga-substituted film (IGO51) was annealed at progressively higher temperatures, quenched to room temperature at each point (the same annealing process used for the crystallization study), and characterized by Hall effect measurements. Note that above 150 °C there is a rapid fall in carrier content to a level one to two orders of magnitude below that of the as-deposited film. Note also that the crystallization temperature for this film is ≈ 450 °C (see Figure 1). Therefore, the decline in carrier content between 150 and 250 °C is not associated with crystallization. Instead, we interpret this behavior as the onset of O exchange/equilibration of defects, similar to the equilibration of O vacancies seen in defect studies of a-IZO^[28] and a-IGZO.^[25] Additionally, a decline in carrier concentration of a-IGO has been seen with increased oxygen content during sputtering.^[16c] Oxygen tracer diffusion measurements show that O exchange and diffusion can take place at 200 °C in a-IGZO films;^[25] theoretical calculations have also shown that vacancies can be neutralized at 200 °C in a-IGZO.^[29]

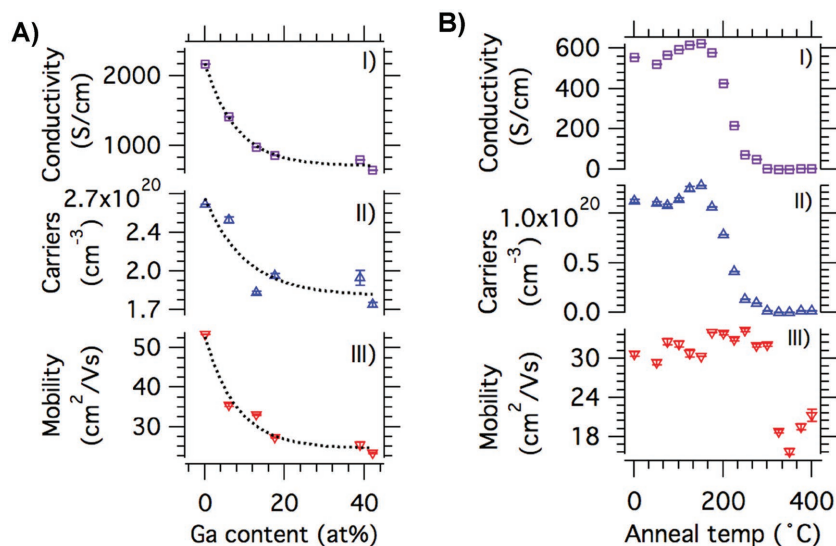


Figure 4. A) Hall effect data for a series of a-IGO thin films as a function of at% Ga. Error bars represent the standard deviation between three samples of the same composition, grown under the same conditions. The error bars are the size of the data points for conductivity and mobility. Dashed lines represent exponential fits of the data and are provided as visual guides for the observed trends. B) Room temperature Hall effect data on IGO51 (blue), as a function of annealing temperature. As-deposited results are plotted at $-25\text{ }^{\circ}\text{C}$. The sample was cycled through air annealing (at increasing temperatures), quench, and room temperature Hall measurements. Error bars are calculated as the standard deviation of 10 consecutive measurements.

2.2.2. Carrier Generation: MD Simulations and Density Functional Theory (DFT) Calculations

As discussed in Section 2.2.1 above, Ga does not serve as a carrier donor in amorphous In–Ga–O. This is supported by the present DFT calculations for stoichiometric amorphous In–Ga–O oxides; independent of the level of fractional Ga substitution, the electronic band structure of a-IGO corresponds to an insulator, i.e., the conduction band is empty. Furthermore, it can be argued that the carrier-producing entities in a-IGO films are only the In–O polyhedra. As discussed in Sections 2.1.1 and 2.1.2, all Ga atoms satisfy their natural coordination with O atoms—in marked contrast to In atoms, the large fraction of which are undercoordinated, $\text{ECN} < 5.0$, Figure 3A and Table 1. The assertion that only In–O polyhedra contribute to carrier production is consistent with the observed behavior of the end-member films in the a-IGO series; a-IO is highly conductive (see Figure 4A), whereas a-Ga–O is known to be highly resistive, i.e., having immeasurably small carrier densities.^[30] Note that, although the undercoordination of In–O polyhedra suggests a role in carrier production, there is not a direct correlation between undercoordination and carrier concentration. Indeed if each instance of undercoordination was the site of a charged O vacancy, the carrier concentration would exceed the experimental values by two orders-of-magnitude.

Accurate DFT calculations on nonstoichiometric a-IO and a-IGO, with the same O stoichiometry of 2.96 for each structure, provide additional insight into the carrier generation mechanism in these materials. It is found that low coordination of In is a necessary, but not a sufficient condition to form a donor defect. The charge density distribution (Figure 5) calculated for

the partially occupied conduction band in a-IO and a-IGO reveals that a notable charge density accumulates in the interstitial region between two or three In neighbors that not only have low coordination ($\text{ECN} = 4.4\text{--}5.0$ for all four compositions considered), but are also undershared, i.e., lack an O atom to form a connection that is expected based on the distance between the corresponding In atoms. In a-IO and in three a-IGO structures with variable Ga content, low-coordinate In polyhedral pairs are separated by a short distance of 3.1–3.5 Å and are corner-shared, missing the additional O atom expected at this separation. Hence, despite the large fraction of low-coordinate In atoms (Figure 3A), only undershared In atoms located at short distances show charge accumulation. Structurally, the pair of undershared, undercoordinated In atoms resembles an O vacancy defect in a crystalline oxide. The difference between what is observed as an O vacancy in crystalline materials and what is observed in our a-IGO models is seen in the range of structural rearrangement that accompanies the O defect. Owing to the many degrees of freedom in the amorphous structure, the entire cell adjusts to accommodate the O

defect during the MD quench process for a-IO and a-IGO—in marked contrast to the local atomic relaxation, i.e., within the nearest and next nearest neighbors only, which occurs around O vacancies in crystalline oxides.

The long-range reconstruction of the amorphous structure in nonstoichiometric oxides limits the influence of secondary cations on carrier production. The theoretical results suggest the cation composition has little effect on the conduction states below the Fermi level. In Figure 6, the calculated inverse participation ratio (IPR) for the occupied states in the conduction band is low, signifying that the defect is shallow and the delocalized nature of the occupied states in the conduction band persists in all 3 a-IGO simulations. This finding is supported by the fact that the Burstein–Moss (BM) shift, i.e., the Fermi level shift into the conduction band, calculated to be 1.41, 1.46, and 1.55 eV in IGO11, IGO19, and IGO41, respectively, is only slightly smaller than the BM shift in a-IO, 1.61 eV, with the same oxygen stoichiometry. Thus, Ga does not change the source of carriers in a-IGO.

The electron concentration calculated from integrated density of states within a 0.2 eV window below the Fermi level is $2.80 \times 10^{20}\text{ cm}^{-3}$, $2.03 \times 10^{20}\text{ cm}^{-3}$, and $2.30 \times 10^{20}\text{ cm}^{-3}$ for 11%, 19%, and 41% of Ga, respectively. The values as well as the trend for the a-IGO series are in excellent agreement with those observed experimentally (Figure 4A). Based on the results of these calculations, the carrier concentration behavior in a-IGO can be explained as follows. In undoped a-IO, the majority of In atoms form a long-range network of octahedrally coordinated In–O polyhedra^[8c] leaving behind O-depleted areas. These oxygen-depleted areas facilitate the formation of the remaining undershared low-coordinated In into pairs,

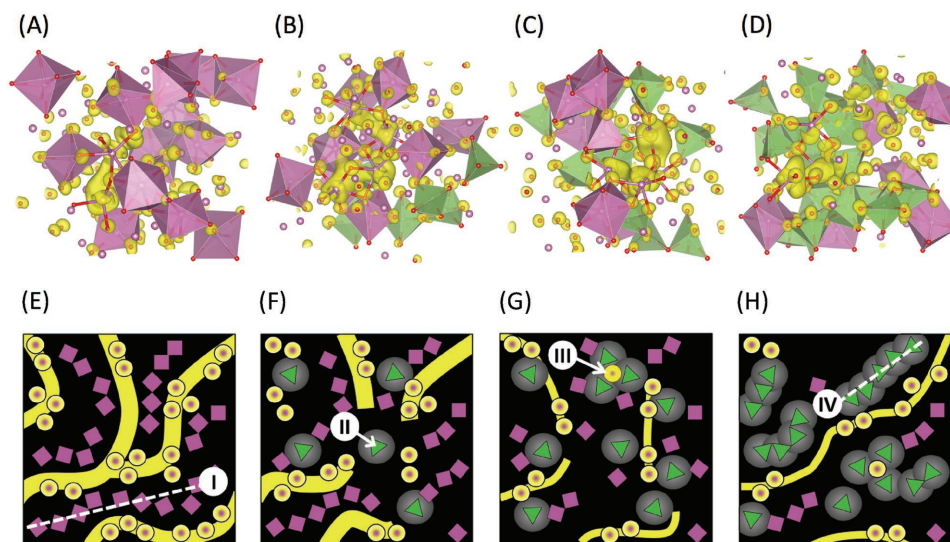


Figure 5. A–D) Calculated charge density distribution in the conduction band of a-IGO. Independent of Ga presence or content, the shallow defect state is associated with the charge accumulation between undershared, low-coordinated, In–In pairs in A) a-IO, B) IGO11, C) IGO19, D) IGO41. In all cases, the charge avoids octahedrally coordinated In–O polyhedra (purple) as well as Ga–O polyhedra (green). For the undershared, low-coordinated In atoms (no polyhedra), the In–O bonds are shown (red-purple). E–H) 2D simplification of the structures for E) a-IO, F) IGO11, G) IGO19, H) IGO41. In–O octahedral, represented as purple squares, form chains (I), which organize undercoordinated In–O polyhedra, represented as purple circles. This organization produces the yellow conduction manifold of high electron density. The conduction manifold begins to break up in the presence of Ga–O tetrahedra (II), represented as green triangles. Traps (III) form when Ga–O tetrahedra surround low-coordinated In atoms. At high Ga content, chains of Ga–O tetrahedra begin to form (IV), negating Ga’s disrupting effect on the conduction manifold.

which generate charge carriers (Figure 5A). Introduction of Ga suppresses the number of six-coordinate In–O polyhedra (Figures 3A and 5A–C,E–G) and also dilutes the In–O lattice; both factors hamper the ability of two or more undercoordinate In atoms to cluster and form a donor defect. When the fraction of Ga increases above 17 at%, a long-range network of fully coordinated Ga–O polyhedra emerges (Figure 6D,H). While not as efficient as the InO₆ chains, this network does re-enable the formation of the O-depleted areas associated with undershared low-coordinate In pairs. At high Ga concentrations, the source of carriers (pairs of low-coordinate In–O polyhedra) is still diluted but it is no longer disrupted. As a result, the carrier concentration is minimally affected by Ga substitution in the range of 17–40 at%, Figure 4A.

2.2.3. Carrier Mobility: Experimental

The observed concomitant reduction of both carrier mobility and carrier concentration as a function of Ga content (Figure 4; Figure S11, Supporting Information) suggests that a-IGO transport is not limited by ionized impurity scattering.^[31] Additional support is seen in the lack of a carrier mobility response to the drop in carrier concentration, occurring upon air annealing between 150 and 250 °C (Figure 4B). There is, however, a sharp fall in mobility above 325 °C; this is attributable to the nucleation of the crystalline phase,^[8c] in the form of nanoscale inclusions, beginning ≈100 °C before the observation of strong diffraction peaks. Previous microscopy studies on a-IO^[8c] and a-IGZO^[32] demonstrated the presence of nanoscale regions of ordering before the onset of X-ray diffraction peaks.

The observation of a well-developed Hall effect suggests that band conduction is at play in the a-IGO system.^[2,14a,d,e] The proposed transport models which incorporate band-conduction typically consider a combination of trap states and percolation barriers as the factors limiting mobility in amorphous oxide semiconductors.^[14a,b,e] From the above discussion, Ga is expected to affect the number and energy of percolation barriers and trap states by changing the O bonding and medium-range order of M–O polyhedra in a-IGO. The first shell structure around Ga is dissimilar to the surrounding In–O matrix (Sections 2.1.1 and 2.1.2), suggesting Ga–O polyhedra may have a higher energy barrier associated with them.^[5a,6,8d,14] Ga also increases the overall structural disorder of the system. A comparison of the PDF of IGO8 (blue) and IGO17 (red) (Figure 2B) illustrates Ga-induced disorder affecting the M···M distances and beyond. Greater disorder and a less relaxed structure has been associated with a greater number of trap states.^[2,8d] The creation of barriers and traps by the addition of Ga is consistent with the observed fall in a-IGO mobility with increasing Ga content observed through Hall measurements (Figure 4C) and in a-IGO TFT performance (Chiang et al.^[11b] and Park et al.).^[16b]

2.2.4. Carrier Mobility: DFT Computation

Electronic structure calculations on amorphous oxides provide microscopic insights into the origins of the complex transport behavior in materials such as a-IGO. Although the presence of additional cations in In-based AOSs does not directly govern the free carrier generation (see Section 2.2.3), composition-induced

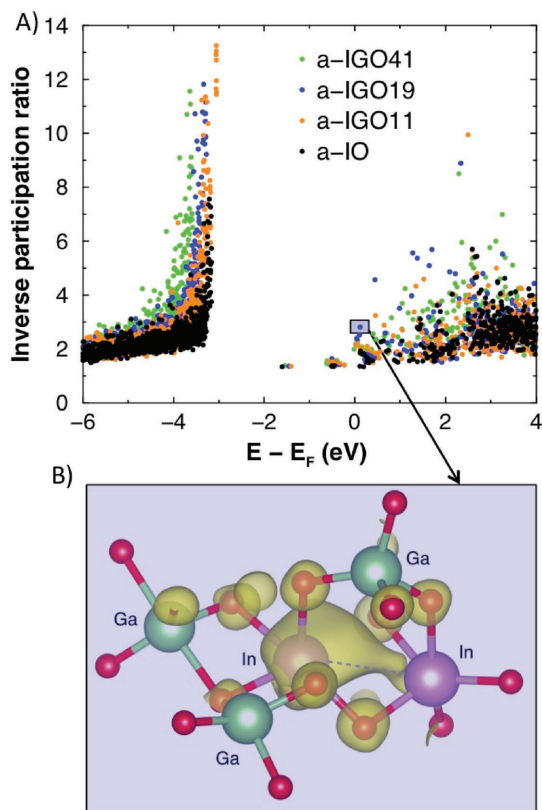


Figure 6. A) The calculated inverse participation ratio for a-IO and a-IGO. The valence band tail states are more localized in IGO than in IO owing to the presence of undercoordinated oxygen atoms. The conduction states below the Fermi level (at 0 eV) are delocalized suggesting the formation of a shallow defect even at high Ga content. Localization of the empty conduction states above the Fermi level associated with nonuniform charge distribution explain the observed mobility drop in a-IGO as compared to a-IO. Above the Fermi level, the charge density is localized at low-coordinate In atom surrounded by fully coordinated Ga atoms as in B) a-IGO19.

differences in the O-sharing and medium-range spatial distribution of the differently coordinated M–O polyhedra affect the carrier mobility. First of all, Ga suppresses the number of octahedrally coordinated In atoms, and hence hampers the formation of shared InO_6 polyhedral chains. The latter have been shown to contribute to high mobility in a-IO:^[8c] Chain formation organizes polyhedra with similar energy states and creates conducting paths along the chains (see Section 2.2.3). Accurate DFT-based hybrid-functional calculations of understoichiometric a-IGO reveal that the electron localization above the Fermi level increases significantly in all three a-IGO structures, as compared to a-IO. This increased localization supports the assertion that Ga inclusion adds to the density of traps. The calculated charge density distribution for the energy slice of 0.5 eV above the Fermi level (unoccupied states) demonstrates (Figure 6) that an extra free electron is likely to be trapped at an undercoordinated In atom surrounded by three fully coordinated Ga atoms. The empty states of the four-coordinate Ga atoms have a higher energy and, hence, are not available for conduction electrons. When the substitutional doping level in

a-IGO increases, clustering of fully coordinated Ga atoms leads to a nonuniform charge density distribution in the conduction states, rendering variable range hopping (VRH),^[29,32] through the states of different energy, the primary conduction mechanism. Indeed, the calculated electron velocity for the states above the Fermi level (the states that form conductivity paths for the free electrons to hop through) decreases from 9.44×10^5 , to 9.35×10^5 , 8.96×10^5 , and 8.42×10^5 m s^{-1} , for amorphous IO and IGO11, IGO19, and IGO41, respectively. Thus, the introduction of Ga affects VRH by increasing the range (distance) between hopping centers.

Once the Ga content approaches 20 at%, Ga has a greater role in the conduction manifold.^[43] At higher Ga contents, the charge localization above the Fermi level decreases as evident from the comparison of the IPR values for IGO19 (blue) and IGO41 (green): the $\text{IPR}(\text{IGO19}) = 4.6$ is nearly two times larger as compared to the $\text{IPR}(\text{IGO41}) = 2.5$ within 0.5 eV above E_F (Figure 5). The weaker localization of the conduction states in a-IGO with higher Ga content is associated with the formation of an extended network of shared Ga–O–Ga polyhedra within the In–O matrix. As with the long chains of InO_6 that organize the low-coordinate In–O polyhedra together (Figure 6A,E and Buchholz^[13]), the formation of shared Ga–O polyhedral chains within the predominantly low-coordinate In–O matrix (Figure 5D,H) again organizes the electron density and establishes two interwoven networks with dissimilar energies. Therefore, it can be argued that above 20 at% Ga in a-IGO, when the structure begins to transform from isolated Ga–O polyhedra to long-range Ga–O chains, the hopping between the low-coordinate In–O states is maintained. This explains the observed unchanged mobility in a-IGO with Ga 20% and above (Figure 4). Thus, the energy and the long-range spatial distribution of the polyhedra ultimately determine the complex behavior of mobility in amorphous IGO.

2.3. Optical Properties: DFT Calculations

Accurate DFT-based hybrid-functional calculations of the real and imaginary dielectric function for amorphous understoichiometric In–Ga–O show that all three compositions demonstrate low optical absorption within the visible range, i.e., for 1.8–3.0 eV. Compared to amorphous indium oxide obtained with the same MD quench rate and the same oxygen stoichiometry up to 18% of substitutional Ga has no effect on the optical absorption edge and the gap remains to be equal to 3.2 eV (see Figure S12, Supporting Information). As expected, larger substitutional fraction of Ga opens up the transparency window: the optical band gap for amorphous $\text{In}_{1.19}\text{Ga}_{0.81}\text{O}_{2.96}$ is 3.5 eV (see Figure S12, Supporting Information).

3. Conclusions

A systematic investigation of the thermal, electrical, and structural properties of a series of amorphous Ga-substituted In–O thin films was performed. Strong agreement between experimental results and theoretical simulations are demonstrated. The results reveal that the thermal instability of a-IO can be

overcome by Ga addition, and the mechanism underlying this effect is identified as the tendency of Ga to maintain the lower coordination, seen in pure Ga–O, even when surrounded by a more highly coordinated In–O matrix. While the coordination and bonding of pure a-IO is fairly close to that of crystalline bixbyte, Ga must undergo significant changes in coordination and bonding before crystallization occurs. The drop in carrier concentration and mobility coincident with Ga substitution was explored. The decline in both properties is shown to wane at Ga >20 at%. Ga dilutes carrier production because it inhibits the formation of undershared low-coordinated In–O polyhedral pairs; these pairs, which are the amorphous equivalent of an O vacancy, are identified as the source of carriers. Ga interrupts carrier mobility because it introduces disorder that leads to increased trap states. In addition, Ga dilutes the In–O polyhedral matrix increasing both the energy and range between variable range hopping centers. At high Ga contents the formation of Ga–O polyhedral chains limits the disrupting effects of Ga on both carrier production and carrier mobility. From a structure–property analysis of a-IGO it is clear that changes in the local and medium-range structure affect all three properties explored here. Future modifications of AOSs through substitutional cations must balance such subtle interwoven effects.

4. Experimental Section

Film Growth: A series of a-IGO thin films was grown by PLD, employing a 248 nm KrF excimer-laser with a pulse duration of 25 ns and a beam energy of 200 mJ per pulse. The beam was focused to a $1 \times 2 \text{ mm}^2$ spot on the target material. Films were grown in a 7.5 mTorr O_2 environment and deposited onto quartz substrates ($1 \times 1 \text{ cm}^2$ and $1 \times 2 \text{ cm}^2$ for local structure measurements). A deposition temperature of $-25 \text{ }^\circ\text{C}$ was chosen to ensure all films would be grown amorphous^[8c] (Figure S1, Supporting Information). Various Ga:In ratios were achieved by alternating ablation between an In_2O_3 target and a Ga_2O_3 target. Less than one monolayer was deposited during each $\text{In}_2\text{O}_3/\text{Ga}_2\text{O}_3$ PLD cycle to insure mixing at the atomic-layer level. To prevent localized heating, the targets were rotated at 5 rpm and the laser beam was rastered radially. The target–substrate distance was fixed at 10 cm.

X-ray fluorescence spectroscopy (XRF) was performed to verify the correct In:Ga atomic ratio achieved in each film. The Ga K and In L fluorescence yields were corrected for their respective XRF cross-sections and detector efficiencies (see Equation S1 of the Supporting Information). Ellipsometry (J. A. Woollam M2000U Ellipsometer) indicated that the films were between 250 and 350 nm thick.

Electrical Characterization: The carrier concentration, carrier mobility, and conductivity of the a-IGO films were measured at room temperature using an Ecopia HMS-3000 Hall measurement system. Gold spring contacts were used in 4-point Van der Pauw configuration. A 0.58 T field was applied using a permanent magnet. I – V curves were collected before each Hall measurement to ensure that Ohmic contact was achieved.

Crystallization Study: Grazing incidence X-ray diffraction (GIXRD) was performed using a Rigaku Smartlab instrument with a multilayer monochromated Cu rotating anode source. GIXRD was used to study the thermally induced film crystallization process. The incident angle of the 8.04 keV X-ray beam was set at 0.4° . The critical angle for In_2O_3 is 0.37° at this energy. A GI geometry was used to avoid scattering from the substrate. To determine the T_{cryst} each film was subjected to a heat–quench–measure cycle. Samples were heated in air for 1.0 h and then quenched to $25 \text{ }^\circ\text{C}$. Heating began at $50 \text{ }^\circ\text{C}$ and was increased in each cycle by $25 \text{ }^\circ\text{C}$ until strong crystalline diffraction peaks could be observed (Figure S1, Supporting Information). This was used to define the T_{cryst} above which no further change in the diffraction pattern is observed.

Short and Medium-Range Structural Characterization: The structures of the a-IGO films were studied using X-ray absorption spectroscopy (XAS) and X-ray scattering techniques. Both X-ray absorption and X-ray scattering measurements were carried out using synchrotron X-rays delivered from the bending magnet 5-BM-D beamline of the DuPont–Northwestern–Dow Collaborative Access Team at the Advanced Photon Source (APS) of Argonne National Laboratory. XAS data were collected in fluorescence mode at the In and Ga K-edges, respectively, using a 4-element Si-drift detector (Vortex-ME4) with DXP-XMAP electronics (XIA LLC). The samples were held vertically and the X-ray incidence angle was set at 54° to ensure that the best average structure was measured. See the Supporting Information for further details on the experimental set up.

For amorphous materials, the XAS measurements reveal, in most cases, only the structure of the nearest neighbor surrounding the atom of interest. In order to probe the structure beyond the first neighbor, GIWAXS measurements at a photon energy of 15.00 keV and anomalous-GIWAXS (A-GIWAXS) measurements around the Ga K edge were carried out. The former produces a PDF of the averaged structure. The latter produces a PDF of the structure around the Ga atoms in the form of a differential (d-)PDF. The grazing incidence angle was set between 0.4° and 0.5° , which was sufficient to remove substrate scattering. See the Supporting Information for further details on the experimental set up.

At 15.00 keV, the GIWAXS data were measured up to $q = 15 \text{ \AA}^{-1}$. For the A-GIWAXS the q -range was limited by the absorption edge energy to $\approx 10.4 \text{ \AA}^{-1}$. The A-GIWAXS technique takes advantage of the significant change in the atomic scattering factor [$f(q, E) = f_0(q) - f'(E) + if''(E)$] around the absorption edge of an element of interest, i.e., Ga in the present work.^[18] Two scattering measurements are needed at different photon energies, one is 100 eV below the Ga K absorption edge (10367 eV) and the other is 2 eV below the edge. The difference of these two measurements yields a difference-pair distribution function (d-PDF) that describes the structure around Ga. Therefore, the A-GIWAXS provides element-specific local structure, similar to XAS.

Data Reduction: For XAS, the data analysis and EXAFS fitting were done using the iXAFS package.^[33] Several photoelectron wavenumber, k , ranges were explored to test the persistence of the results. Fittings of the first shell structure were carried out in real space in the R -range of 1.0–2.3 \AA and 1.0–2.4 \AA for the Ga and In K-edges, respectively. Data in the k -range of 2.59–13.31 \AA^{-1} for the Ga K-edge and in the k -range of 2.29–12.43 \AA^{-1} for the In K-edge, were used. The amplitude reduction factors, S_0^2 , of 0.98 for the Ga K-edge and 1.04 for the In K-edge were determined from fits of the two crystalline reference samples (In_2O_3 and Ga_2O_3).

For GIWAXS, the measured scattering intensities, I_m , were scaled (using scaling factor B) to the atomic scattering intensity, f^2 , in electron units [$I_m \times B = (f^2 + I_{\text{ine}})$] using the so-called high-angle method^[34]—the region where scattering modulations are vanishing. From here, the structure factor, $S(q)$, or interference function was obtained [$S(q) - 1 = [I_e - \{(f^2 + I_{\text{ine}})\}]/(f^2)$] whose Fourier transform yields the PDF. I_e and I_{ine} are the elastic and inelastic intensities, respectively. Both f_0 and I_{ine} were obtained using tabulated values^[35] while $f'(E)$ was obtained by performing the Kramers–Kronig inversion of $f''(E)$, which was measured on the a-IGO film through the absorption channel. For A-GIWAXS, the data processing procedure is similar, except that the K_β emission intensity is removed from the measured scattered intensity, since it is unresolved when the measuring energies are close to the absorption edge. After that it is straightforward to obtain a differential structure factor, $d-S(q)$, the Fourier transform of which yields the d-PDF, which is the probability of finding an atom at distance R from a Ga atom.

Theoretical Methods: The amorphous oxide structures were generated using first-principles MD liquid-quench simulations as implemented in the Vienna ab initio simulation package (VASP).^[36] The calculations are based on the DFT^[37] with periodic boundary conditions and employ the PBE (Perdew–Burke–Ernzerhof) functional^[38] within the projector augmented-wave method.^[39] A bixbyite cell of In_2O_3 with crystalline density of 7.12 g cm^{-3} and with 134 atoms per cell was used as initial structure which was melted at 3000 K to eliminate any crystalline

memory. For Ga-doped indium oxide, random In atoms were substituted with a specific fraction of Ga (11%, 19%, or 41%) and the cell density was adjusted prior to additional melting at 3000 K for 10 ps to randomize the multicomponent configuration. To model nonstoichiometric structures, oxygen atom(s) were randomly removed from the melt prior to additional melting. Next, liquid quench simulations were performed as follows. Each structure was cooled to 1700 K at the MD rate of 100 K ps⁻¹ and then rapidly quenched to 100 K at 200 K ps⁻¹ rate. An energy cut-off of 260 eV and single Γ point were used during melting and quenching processes. Finally, each structure was equilibrated at 300 K for 10 ps with a cut-off energy of 400 eV. All MD simulations were carried out in the NVT (canonical) ensemble with the Nose–Hoover thermostat using an integration time step of 2 fs.

To compare the structural characteristics of the theoretically modeled amorphous oxides to those observed experimentally, room-temperature In–Ga–O structures were used. For an accurate structural analysis of the theoretically modeled amorphous oxides, the average pair correlation function and the average ECN were calculated according to ref. [40]. ECN is calculated for every metal atom by assigning weight to each bond with respect to the shortest M–O bond in the given MO polyhedron. The resulting atomic structures were plotted using VESTA software.^[41]

Next, the atomic configurations obtained from the ab initio MD simulations were optimized at 0 K using the PBE functional. For the optimization, the cut-off energy of 500 eV and the $4 \times 4 \times 4$ Γ -centered k-point mesh were used; the atomic positions were relaxed until the Hellmann–Feynman force on each atom was below 0.01 eV Å⁻¹. The electronic and optical properties of the optimized amorphous In-based oxides were calculated using the hybrid Heyd–Scuseria–Ernzerhof (HSE06) approach^[42] with a mixing parameter of 0.25 and a screening parameter μ of 0.2 Å⁻¹. To characterize the localization of the electronic states within the band gap and near the band edges, the IPR was calculated. Optical absorption was derived from the frequency-dependent dielectric function, $\epsilon(\omega) = \epsilon_1(\omega) + i\epsilon_2(\omega)$, calculated within independent particle approximation as implemented in VASP. The imaginary part, $\epsilon_2(\omega)$, is related to the optical absorption at a given frequency, ω , and is determined based on the electronic transitions of the hybrid functional solution. The real part of the complex dielectric function is obtained using Kramers–Kronig relations.

Supporting Information

Supporting Information is available from the Wiley Online Library or from the author.

Acknowledgements

This work was supported by the NSF MRSEC Program No. DMR 1121262 at the Materials Research Center of Northwestern University (NU). This work made use of the J. B. Cohen X-Ray Diffraction Facility and the MatCI Facilities at NU, supported by the MRSEC program of the National Science Foundation (NSF) and NU. Ellipsometry was performed in the Keck-II facility of the NUANCE Center at NU. NSF-NSEC, NSF-MRSEC, Keck Foundation, the State of Illinois, and NU support the NUANCE Center. DND-CAT is supported through NU, E. I. DuPont de Nemours & Co., The Dow Chemical Co., the State of Illinois through the Department of Commerce and the Board of Education (HECA), the US Department of Energy Office of Energy Research, and the US National Science Foundation (NSF) Division of Materials Research. The Department of Energy (DOE) under grant number DE-AC02-06CH11357 supports Argonne National Laboratory. Computational resources were provided by the NSF-supported XSEDE program and by DOE NERSC facilities. S.L.M. acknowledges support of a NSF Graduate Research Fellowship.

Conflict of Interest

The authors declare no conflict of interest.

Keywords

amorphous semiconductors, conductivity, local structure, oxides

Received: May 4, 2017

Revised: June 28, 2017

Published online:

- [1] E. Fortunato, A. Pimentel, L. Pereira, A. Gonçalves, G. Lavareda, H. Águas, I. Ferreira, C. N. Carvalho, R. Martins, *J. Non-Cryst. Solids* **2004**, 338–340, 806.
- [2] A. Takagi, K. Nomura, H. Ohta, H. Yanagi, T. Kamiya, M. Hirano, H. Hosono, *Thin Solid Films* **2005**, 486, 38.
- [3] a) E. Fortunato, P. Barquinha, R. Martins, *Adv. Mater.* **2012**, 24, 2945; b) J. F. Wager, B. Yah, R. L. Hoffman, D. A. Keszler, *Curr. Opin. Solid State Mater. Sci.* **2014**, 18, 53; c) T. Kamiya, K. Nomura, H. Hosono, *Sci. Technol. Adv. Mater.* **2010**, 11, 044305; d) X. Yu, T. J. Marks, A. Facchetti, *Nat. Mater.* **2016**, 15, 383.
- [4] a) R. Martins, P. Barquinha, I. Ferreira, L. Pereira, G. Gonçalves, E. Fortunato, *J. Appl. Phys.* **2007**, 101, 044505; b) H. Hosono, *J. Non-Cryst. Solids* **2006**, 352, 851.
- [5] a) K. Nomura, H. Ohta, A. Takagi, T. Kamiya, M. Hirano, H. Hosono, *Nature* **2004**, 432, 488; b) H. Hosono, N. Kikuchi, N. Ueda, H. Kawazoe, *J. Non-Cryst. Solids* **1996**, 198–200, 165.
- [6] P. K. Song, H. Akao, M. Kamei, Y. Shigesato, I. Yasui, *Jpn. J. Appl. Phys.* **1999**, 38, 5224.
- [7] S. Parthiban, J.-Y. Kwon, *J. Mater. Res.* **2014**, 29, 1585.
- [8] a) A. Yan, T. Sun, K. B. Borisenko, D. B. Buchholz, R. P. H. Chang, A. I. Kirkland, V. P. Dravid, *J. Appl. Phys.* **2012**, 112, 054907; b) Divya, R. Prasad, Deepak, *Phys. Status Solidi a* **2017**, 214, 1600471; c) D. B. Buchholz, Q. Ma, D. Alducin, A. Ponce, M. Jose-Yacamán, R. Khanal, J. E. Medvedeva, R. P. H. Chang, *Chem. Mater.* **2014**, 26, 5401; d) J. Smith, L. Zeng, R. Khanal, K. Stallings, A. Facchetti, J. E. Medvedeva, M. J. Bedzyk, T. J. Marks, *Adv. Electron. Mater.* **2015**, 7, 1500146.
- [9] a) S. J. L. Billinge, M. G. Kanatzidis, *Chem. Commun.* **2004**, 749; b) Q. Zhu, Q. Ma, D. B. Buchholz, R. P. H. Chang, M. J. Bedzyk, T. O. Mason, *J. Appl. Phys.* **2014**, 115, 033512.
- [10] K. Nomura, T. Kamiya, H. Ohta, T. Uruga, M. Hirano, H. Hosono, *Phys. Rev. B: Condens. Matter Mater. Phys.* **2007**, 75, 2.
- [11] a) M. P. Taylor, D. W. Readey, C. W. Teplin, M. F. A. M. van Hest, J. L. Alleman, M. S. Dabney, L. M. Gedvilas, B. M. Keyes, B. To, J. D. Perkins, D. S. Ginley, *Meas. Sci. Technol.* **2004**, 16, 90; b) H. Q. Chiang, D. Hong, C. M. Hung, R. E. Presley, J. F. Wager, C. H. Park, D. A. Keszler, G. S. Herman, *J. Vac. Sci. Technol., B: Microelectron. Nanometer Struct.–Process., Meas., Phenom.* **2006**, 24, 2702; c) S. Jeong, Y.-G. Ha, J. Moon, A. Facchetti, T. J. Marks, *Adv. Mater.* **2010**, 22, 1346; d) D. E. Proffitt, T. Philippe, J. D. Emery, Q. Ma, D. B. Buchholz, P. W. Voorhees, M. J. Bedzyk, R. P. H. Chang, T. O. Mason, *J. Electroceram.* **2015**, 34, 167.
- [12] a) T. Kamiya, K. Nomura, H. Hosono, *Phys. Status Solidi* **2010**, 207, 1698; b) Y. H. Kang, S. Jeong, J. M. Ko, J.-Y. Lee, Y. Choi, C. Lee, S. Y. Cho, *J. Mater. Chem. C* **2014**, 2, 4247; c) M.-H. Kim, M.-J. Choi, K. Kimura, H. Kobayashi, D.-K. Choi, *Solid-State Electron.* **2016**, 126, 87; d) Y. G. Kim, T. Kim, C. Avis, S.-H. Lee, J. Jang, *IEEE Trans. Electron Devices* **2016**, 63, 1078; e) S. Bubel, M. L. Chabiny, *J. Appl. Phys.* **2013**, 113, 234507.

- [13] a) D. Kang, H. S. Lee, J.-W. Park, S. H. Baek, S.-H. Choi, H. Lee, *Appl. Phys. Lett.* **2007**, *91*, 091910; b) M. Orita, H. Ohta, M. Hirano, H. Hosono, *Appl. Phys. Lett.* **2000**, *77*, 4166; c) H. Kostlin, R. Jost, W. Lems, *Phys. Status Solidi* **1975**, *29*, 87.
- [14] a) T. Kamiya, K. Nomura, H. Hosono, *Appl. Phys. Lett.* **2010**, *96*, 122103; b) P.-Y. Liao, T.-C. Chang, T.-Y. Hsieh, M.-Y. Tsai, B.-W. Chen, Y.-H. Tu, A.-K. Chu, C.-H. Chou, J.-F. Chang, *Jpn. J. Appl. Phys.* **2015**, *54*, 094101; c) W. Chr. Germs, W. H. Adriaans, A. K. Tripathi, W. S. C. Roelofs, B. Cobb, R. A. J. Janssen, G. H. Gelinck, M. Kemerink, *Phys. Rev. B* **2012**, *86*, 155319; d) I. I. Fishchuk, A. Kadashchuk, A. Bhooklam, A. de Jamblinne de Meux, G. Pourtois, M. M. Gavriluk, A. Kohler, H. Bassler, P. Heremans, J. Genoe, *Phys. Rev. B* **2016**, *93*, 195204; e) A. Bhoolakam, M. Nag, S. Steudel, J. Genoe, G. Gelinck, A. Kadashchuk, G. Groeseneken, P. Heremans, *Jpn. J. Appl. Phys.* **2016**, *55*, 014301.
- [15] T. Kamiya, K. Nomura, H. Hosono, *Phys. Status Solidi* **2009**, *206*, 860.
- [16] a) C.-H. Choi, Y.-W. Su, L.-Y. Lin, C.-C. Cheng, C.-H. Chang, *RSC Adv.* **2015**, *5*, 93779; b) J. H. Park, W. J. Choi, S. S. Chae, J. Y. Oh, S. J. Lee, K. M. Song, H. K. Baik, *Jpn. J. Appl. Phys.* **2011**, *50*, 080202; c) G. Gonçalves, P. Barquinha, L. Pereira, N. Franco, E. Alves, R. Martins, E. Fortunato, *Electrochem. Solid-State Lett.* **2010**, *13*, H20.
- [17] M. Ramzan, T. Kaewmaraya, R. Ahuja, *Appl. Phys. Lett.* **2013**, *103*, 072113.
- [18] P. H. Fuoss, P. Eisenberger, W. K. Warburton, A. Bienenstock, *Phys. Rev. Lett.* **1981**, *46*, 1537.
- [19] M. Marezio, *Acta Crystallogr.* **1965**, *20*, 723.
- [20] S. Geller, *J. Chem. Phys.* **1960**, *33*, 676.
- [21] L. Pauling, *J. Am. Chem. Soc.* **1929**, *51*, 1010.
- [22] a) F. Utsuno, H. Inoue, Y. Shimane, T. Shibuya, K. Yano, K. Inoue, I. Hirose, M. Sato, T. Honma, *Thin Solid Films* **2008**, *516*, 5818; b) C. A. Hoel, S. Xie, C. Benmore, C. D. Malliakas, J.-F. Gaillard, K. R. Poeppelmeier, *Zeitschrift Anorganische Allgemeine Chemie* **2011**, *637*, 885.
- [23] Q. Zhu, *Ph.D.*, Northwestern University, Evanston, IL **2013**.
- [24] D. D. Edwards, P. E. Folkins, T. O. Mason, *J. Am. Ceram. Soc.* **1997**, *80*, 253.
- [25] A. U. Adler, T. C. Yeh, D. B. Buchholz, R. P. H. Chang, T. O. Mason, *Appl. Phys. Lett.* **2013**, *102*, 122103.
- [26] J. E. Medvedeva, R. Khanal, *Vacuum* **2015**, *114*, 142.
- [27] a) E. Fortunato, A. Gonçalves, A. Marques, A. Viana, H. Águas, L. Pereira, I. Ferreira, P. Vilarinho, R. Martins, *Surf. Coat. Technol.* **2004**, *180–181*, 20; b) V. Assunção, E. Fortunato, A. Marques, H. Águas, I. Ferreira, M. E. V. Costa, R. Martins, *Thin Solid Films* **2003**, *427*, 401.
- [28] a) S. Lee, D. C. Paine, *Appl. Phys. Lett.* **2013**, *102*, 052101; b) S. L. Moffitt, A. U. Adler, T. Gennett, D. S. Ginley, J. D. Perkins, T. O. Mason, *J. Am. Ceram. Soc.* **2015**, *98*, 2099.
- [29] B. Ryu, H.-K. Noh, E.-A. Choi, K. J. Chang, *Appl. Phys. Lett.* **2010**, *97*, 1.
- [30] L. Nagarajan, R. A. De Souza, D. Samuels, I. Valov, A. Borger, J. Janek, K.-D. Becker, P. C. Schmidt, M. Martin, *Nat. Mater.* **2008**, *7*, 391.
- [31] B. Streetman, S. Banerjee, *Solid State Electronic Devices*, Prentice Hall Inc., Upper Saddle River, NJ, USA **2000**.
- [32] K. Ide, K. Nomura, H. Hiramatsu, T. Kamiya, H. Hosono, *J. Appl. Phys.* **2012**, *111*, 073513.
- [33] B. Ravel, M. Newville, *J. Synchrotron Res.* **2005**, *12*, 537.
- [34] H. Klug, L. Alexander, *X-ray Diffraction Procedures: For Polycrystalline and Amorphous Materials*, John Wiley, New York, NY, USA **1974**.
- [35] a) N. G. Alexandropoulos, M. J. Cooper, P. Suortti, B. T. M. Willis, *International Tables for Crystallography*, John Wiley & Sons, Hoboken, NJ **2006**; b) D. Waasmaier, A. Kirfel, *Acta Crystallogr.* **1994**, *A51*, 416.
- [36] a) G. Kresse, J. Hafner, *Phys. Rev. B* **1993**, *47*, 558; b) G. Kresse, J. Hafner, *Phys. Rev. B* **1994**, *49*, 14251; c) G. Kresse, J. Furthmiller, *Comput. Mater. Sci.* **1996**, *6*, 15; d) G. Kresse, J. Furthmiller, *Phys. Rev. B* **1996**, *54*, 11169.
- [37] a) W. Khon, L. J. Sham, *Phys. Rev. B* **1965**, *140*, A1133; b) P. Hohenberg, W. Kohn, *Phys. Rev.* **1964**, *136*, B864.
- [38] a) J. P. Perdew, K. Burke, M. Ernzerhof, *Phys. Rev. Lett.* **1996**, *77*, 3865; b) J. P. Perdew, K. Burke, M. Ernzerhof, *Phys. Rev. Lett.* **1996**, *78*, 1396.
- [39] a) G. Kresse, D. Joubert, *Phys. Rev. B* **1999**, *59*, 1758; b) P. E. Blochl, *Phys. Rev. B* **1994**, *50*, 17953.
- [40] a) R. Hoppe, *Angew. Chem. Int. Ed.* **1970**, *9*, 25; b) R. Hoppe, S. Voigt, H. Glaum, J. Kissel, H. P. Muller, K. Bernet, *J. Less-Common Met.* **1989**, *156*, 105; c) R. Khanal, D. B. Buccholz, R. P. H. Chang, J. E. Medvedeva, *Phys. Rev. B* **2015**, *91*, 205203.
- [41] F. I. Koichi Momma, *J. Appl. Cryst.* **2011**, *44*, 1272.
- [42] a) J. Heyd, G. E. Scuseria, M. Ernzerhof, *J. Chem. Phys.* **2003**, *118*, 8207; b) J. Heyd, J. E. Peralta, G. E. Scuseria, R. L. Martin, *J. Chem. Phys.* **2005**, *123*, 174101.
- [43] M. Orita, H. Ohta, M. Hirano, S. Narushima, H. Hosono, *Philos. Mag. B* **2001**, *81*, 501.